Supporting Information for

Bacterial magnetofossil evidence for enhanced Pacific Ocean respired carbon storage during buildup of Antarctic glaciation

Dunfan Wang[1,2], Yihui Chen[3], Yan Liu[4], Andrew P. Roberts[5], Eelco J. Rohling[6,7], Xiangyu Zhao[8], Xu Zhang[9], Jinhua Li[4], Weiqi Yao[2], Xuejiao Qu[1], Xianfeng Tan[1*], Qingsong Liu[2*]

[1]*College of Petroleum and Gas Engineering, Chongqing University of Science and Technology, Chongqing 401331, China.*

[2]*Centre for Marine Magnetism (CM[2]), Department of Ocean Science and Engineering, Southern University of Science and Technology, Shenzhen 518055, China.*

[3]*Department of Atmospheric and Ocean Science, School of Physics, Peking University, Beijing 100871, China.*

[4]*Key Laboratory of Earth and Planetary Physics, Institute of Geology and Geophysics, Innovation Academy for Earth Sciences, Chinese Academy of Sciences, Beijing, China.*

[5]*Research School of Earth Sciences, Australian National University, Canberra ACT 2601, Australia.*

[6]*Department of Earth Sciences, Utrecht University, Princetonlaan 8, 3584 CB Utrecht, The Netherlands.*

[7]*Ocean and Earth Science, University of Southampton, National Oceanography Centre, Southampton SO13 3ZH, UK.*

[8]*School of Oceanography, Shanghai Jiao Tong University, Shanghai 200030, China.*

[9]*Group of Alpine Paleoecology and Human Adaptation (ALPHA), State Key Laboratory of Tibetan Plateau Earth System, Resources and Environment (TPESRE), Institute of Tibetan Plateau Research, Chinese Academy of Sciences, Beijing, China*

***Corresponding authors**: Qingsong Liu (qsliu@sustech.edu.cn, +86 0755-88018789)

Xianfeng Tan (xianfengtan8299@163.com, 023-65023057)

Contents of this file
Text S1-S3
Figure S1-S2
Table S1

Introduction

This supporting information includes details of materials and studied sites (Text S1), magnetic and geochemical analytical methods (Text S2), model configuration and boundary conditions for climate simulation experiments (Text S3), sea-ice fraction simulation results (Figure S1), the age model adopted for the studied sites (Figure S2), and parameters associated with components identified from isothermal remanent magnetization (IRM) unmixing analysis (Table S1), as discussed in the main text.

Text S1. Materials and studied sites

In this study, we collected 165 discrete sediment samples in total from cores U1333B-1H to 16 H (~140 m thick sequence at ~2 m stratigraphic intervals) and 1218A-12H to 27X (~200 m thick sequence at ~2 m stratigraphic intervals) from IODP Site 1333 and ODP Site 1218. Sites 1333 (10°30.996′ N, 138°25.159′ W, water depth 4861 m) and 1218 (8°53.366′ N, 135°22.002′ W, water depth 4826 m) are located in the present-day high-nutrient, low-chlorophyll (HNLC) region in the eastern equatorial Pacific (EEP) Ocean (Figure 1A), which recovered Eocene to Miocene sediments within the Intertropical Convergence Zone (ITCZ) region (Wang et al., 2023). Sediment lithologies consist mostly of nannofossil oozes and chalks, with varying aeolian dust proportions from the Asian interior and biogenic magnetofossil enrichments (Pälike et al. 2010). Sediments ages were obtained by linear interpolation from the age model of Westerhold et al. (2012).

Surface-water divergence driven largely by Southern Hemisphere westerlies causes Antarctic circumpolar water (ACC) upwelling toward the surface, advecting nutrients that fuel Southern Ocean biological productivity (Russell, 2023). Part of the sinking dead biomass reaches and respires in Antarctic Bottom Water (AABW), which refreshes the abyssal ocean (below 4,000 metres) and conveys dissolved inorganic carbon into the wider ocean interior, including the deep Pacific Ocean (Figure 1B). Southern Ocean biological pump variations, thus, can drive fluctuations in a vast deep Pacific Ocean respired carbon pool, with substantial implications for global climate (Jian et al., 2023; Jacobel et al., 2017). Our two studied sites are both below the carbonate compensation depth along the AABW flow pathway and are, thus, suitable for tracing deep Pacific Ocean deoxygenation, which relates to Southern Ocean production variations (Coxall et al., 2005).

Text S2. Magnetic and geochemical analytical methods

Bulk magnetic measurements on sediment samples were performed to characterize the domain state, coercivity (B_c), and magnetic mineral concentration. Given that magnetofossils dominate magnetic mineral assemblages (> 95% contribution to sediment magnetization) and high coercivity eolian dust input declined after the EOT at the studied sites (Wang et al., 2023), we conclude that bulk sediment B_c mainly reflects the average coercivity of sedimentary magnetofossils in our study. Isothermal remanent magnetization (IRM) and first-order reversal curves (FORCs) were measured for all studied samples on a 3900 Series vibrating sample magnetometer (Lake Shore Cryotronics, Inc) following Egli (2004) and Roberts et al. (2000), respectively. To estimate the relative magnetofossil content, we measured the anhysteretic remanent magnetization (ARM) after alternating field demagnetization at 20 mT ($ARM_{@20\ mT}$), which is sensitive to the stable SD

ferrimagnetic particle concentration in sediments. ARM was imparted by superimposing a 0.05 mT direct current bias field on a smoothly decreasing 100 mT peak alternating field, which was then demagnetized with a 20 mT peak AF to obtain $ARM_{@20\ mT}$. $ARM_{@20\ mT}$ effectively excludes MD or vortex state particle influences that contribute to the partial ARM below 20 mT, and provide a more reliable measure of SD particle content in the studied samples (Liu et al., 2005). To check for carbonate dilution effects, $ARM_{@20\ mT}$ results are normalized on a carbonate-free basis (CFB) by the (1 – $CaCO_3$ content).

Magnetic extraction was carried out following Li et al. (2020). First, about ~0.5 mg of sediment was suspended into ~50 ml of Milli-Q water in a ~100 ml beaker and was then mixed by ultrasonication assisted by agitation with a glass stirring rod. Second, a 5 × 5 mm cylindrical neodymium magnet (surface field strength > 100 mT) was attached to the outside of the beaker ~2 mm above the water-sediment surface. After ~4 h, magnetic minerals that were concentrated adjacent to the magnet were transferred to a 10 ml glass tube. To extract as much of the magnetic mineral content from the sediment as possible, the first and second steps were repeated several times until no obvious magnetic aggregates were found adjacent to the magnet. Third, extracted magnetic minerals were resuspended in ~5 ml of Milli-Q water in a 10 ml glass tube, mixed by ultrasonication, and then extracted magnetically again following a similar procedure as the second step above. To remove non-magnetic minerals from the extracts, the third step was repeated several times until non-magnetic particles were not observed at the bottom of the tube. The final three repeats were performed in 99.5% ethanol. Finally, extracted magnetic minerals were suspended in 50 μl of 99.5% ethanol and were stored at −20°C before undertaking transmission electron microscope (TEM) observations.

Biogenic silica (opal) was measured using the timed-dissolution technique (Mortlock and Froelich, 1989). About 50 mg of powder sample was placed into a 50 ml tube, 40 ml of 0.2 mol/l sodium carbonate solution was added, and the mixture was heated at 85℃ for 6 hours with shaking every 2 hours. The remaining mixture was centrifuged at 4,000 revolutions/minute for 5 minutes and 100-400 µl of supernatant was taken immediately for analysis, with addition of 4 ml of deionized water and 2 ml of ammonium molybdate acid solution, followed by shaking and reacting for 10 minutes. Then, 2 ml of oxalic acid solution (100 g/l) was added, followed by addition of 4 ml of ascorbic acid solution (1.5%) to a constant 25 ml volume. After 1 hour, samples were analysed in the spectrophotometer with 812 nm wavelength. The standard deviation for analyses is < 4%.

Geochemical elements were measured with IRIS Intrepid II XSP ICP-OES and Varian 820 ICP-MS systems, respectively. Samples (0.04 g) were weighed precisely in a Teflon cup before adding 1.5 ml of HF and 0.5 ml of HNO_3. After digestion in an oven at 180℃ for 12 hours, samples were removed and placed on a hot plate (150℃) to dry. Subsequently, 1 ml of HNO_3 and 1ml of deionized water were added. After 12 hours of airtight digestion at 150℃, samples were cooled, and were then weighed and diluted to 40 g (dilution ratio of 1,000) for analysis. The relative error of major and trace element results is < 2% and < 5%, respectively. To calculate the biogenic "excess" Ba (xsBa) concentration in sediment samples, which mainly represents export productivity, we excluded the detrital Ba component, which is estimated by multiplying the detrital Th concentration by the average upper crustal Ba/Th ratio of 51.4 (Taylor & McLennan, 1985).

Sediment ages were obtained by linear interpolation using the revised age model of Westerhold et al. (2012). Opal, xsBa, and $ARM_{@20\ mT}$ fluxes were calculated by

multiplication with the mass accumulation rate (MAR), where MAR = density * LSR (linear sedimentation rate).

Text S3. Model configuration and boundary conditions for climate simulation experiments

Climate simulations were carried out with the coupled Community Earth System Model (CESM1.2.2). CESM1.2.2 is a general circulation model with seven components: atmosphere, ocean, land, river runoff, sea ice, land ice, and ocean waves, which interact with each other through a coupler (Craig et al., 2012). The resolution of the atmospheric component, Community Atmosphere Model version 4 (CAM4; Neale et al., 2013), is 3.75° in longitude by 3.75° in latitude, with 26 vertical levels. The land component, Community Land Model version 4 (CLM4; Lawrence et al., 2012), has the same horizontal resolution as CAM4. The River Transport Model (RTM) directs all runoff to the oceans and is run with the default resolution (0.5° × 0.5°). The runoff direction for each land grid cell is computed based on surface topography so that water flows downhill without interior drainage loops. The ocean component, Parallel Ocean Program version 2 (POP2; Danabasoglu et al., 2012), has a nominal 3° irregular horizontal grid (116 and 100 grid points in the meridional and zonal directions, respectively), with 60 vertical levels. The sea ice component, Community Sea Ice Model version 4 (CICE4; Hunke & Lipscomb, 2010), is run on the same horizontal grid as POP2.

The simulations are based on the EOT climate state using the global paleogeography at 35 Ma modified from Scotese and Wright (2018). To constrain climate feedback from vegetation, we prescribed that the global vegetation distribution is the same as in the EOT simulation. The eccentricity of Earth's orbit is fixed at 0 and obliquity at 23.5°, which is

nearly the average condition on orbital timescales. The solar constant is scaled to 1357.3 Wm^{-2}, which is ~0.27% lower than the present-day value of 1361 Wm^{-2} (Gough, 1981). A sustained CO_2 decrease has been hypothesized as a potential EOT cooling mechanism (Hutchinson et al., 2021). CO_2 concentrations are set to 1120 ppm in the pre-EOT simulation based on geological evidence (Rae et al., 2021). The pre-EOT simulation was spun up for about 8,000 model years until climate equilibrium was approached. The post-EOT experiment represents a CO_2 decrease from 1120 to 560 ppm, which was branched from the 8001st restart of the pre-EOT simulation and continued to run for 8000 model-years (Goldner et al., 2014). We used a fully coupled General Circulation Model (GCM) to simulate the EOT. CFC concentrations were set to 0, and CH_4 and N_2O were set to 760 and 270 ppbv, respectively.

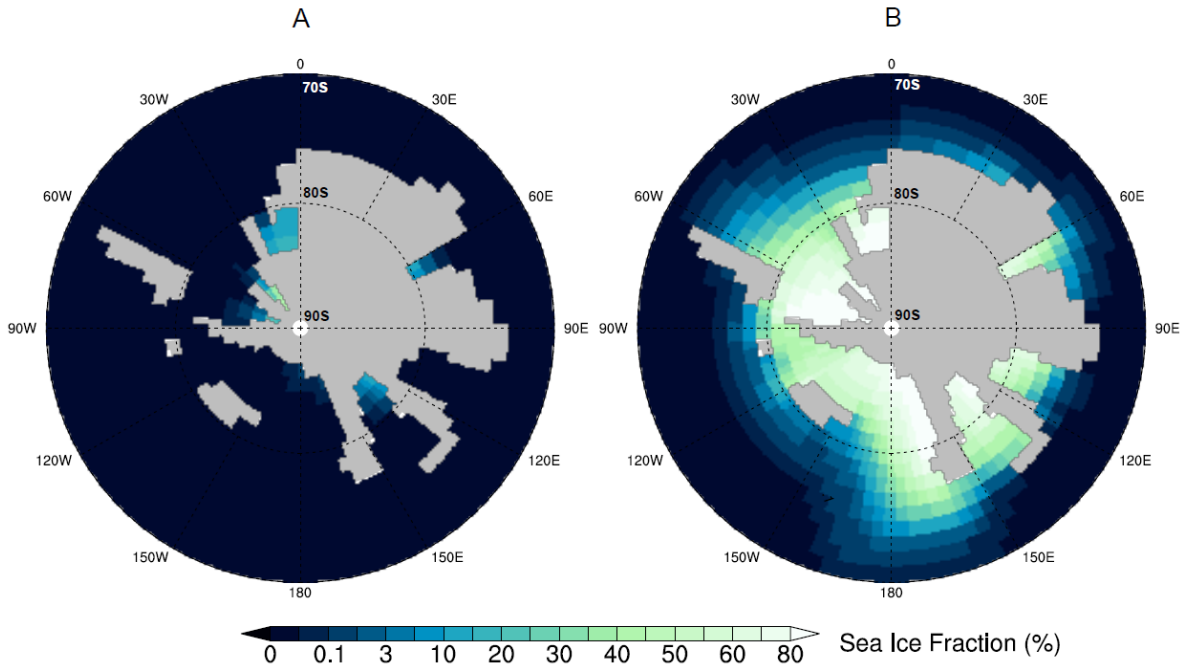

Figure S1. Simulations of sea ice fraction with pCO_2 of (A) 1120 ppm and (B) 560 ppm.

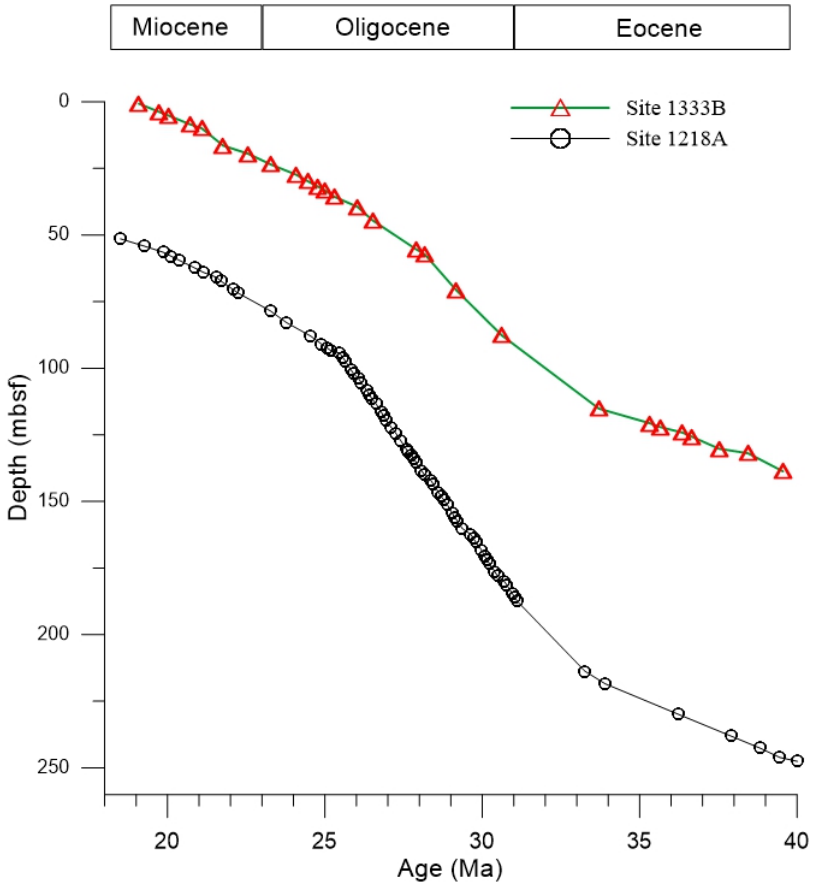

Figure S2. Age model for Sites U1333 and 1218 based on magnetic polarity stratigraphy from Westerhold et al. (2012).

Table S1. IRM unmixing results for representative samples. Components 1 and 4 represent eolian magnetic materials with low and high coercivity. Components 2 and 3 represent the biogenic soft (BS) and biogenic hard (BH) components of Egli (2004), respectively. DP is the dispersion parameter for the distribution.

Sample	Component 1	Component 2	Component 3	Component 4
U1333B (Ma)		Content percentage (%)		
1H-4 (20.04)	17.2	58.1	15.8	8.9
2H-5 (21.56)	17.8	57.4	15.8	8.9
3H-2 (22.56)	17.9	56.4	17.4	8.2
7H-2 (28.16)	16.7	59.6	16.3	7.4
10H-2 (30.47)	17.6	56.9	18.6	6.9

11H-5 (32.00)	16.7	57.8	17.6	7.8
12H-1 (32.39)	16.7	59.5	15.9	7.9
12H-5 (33.06)	17.7	58.2	16.1	8.0
13H-2 (33.71)	16.9	59.5	15.4	8.2
13H-3 (33.93)	17.1	65.3	8.6	9.0
13H-6 (35.33)	17.0	65.1	8.3	9.6
14H-2 (36.36)	17.1	66.8	7.4	8.7
14H-5 (37.18)	17.2	68.0	6.9	7.9
15H-1 (38.45)	18.8	71.2	6.0	4.0
16H-1 (39.91)	18.2	72.7	5.1	4.0
U1333 (Ma)			$B_{1/2}$ (mT)	
1H-4 (20.04)	12.6	32.4	64.6	213.8
2H-5 (21.56)	12.6	31.6	66.1	213.8
3H-2 (22.56)	12.3	31.6	63.1	213.8
7H-2 (28.16)	12.3	31.6	61.7	204.2
10H-2 (30.47)	13.5	32.5	63.1	213.8
11H-5 (32.00)	12.6	32.4	63.1	213.8
12H-1 (32.39)	12.9	33.1	62.3	218.8
12H-5 (33.06)	12.6	31.6	63.1	218.8
13H-2 (33.71)	12.0	32.4	63.1	218.8
13H-3 (33.93)	12.3	32.7	64.6	208.9
13H-6 (35.33)	12.4	30.9	63.1	204.2
14H-2 (36.36)	12.3	30.2	61.7	199.5
14H-5 (37.18)	12.3	31.6	60.3	169.8
15H-1 (38.45)	13.2	31.6	60.3	208.9
16H-1 (39.91)	12.4	30.2	60.3	204.2
U1333 (Ma)			Dispersion parameter (DP)	
1H-4 (20.04)	0.33	0.19	0.19	0.31
2H-5 (21.56)	0.34	0.18	0.15	0.33
3H-2 (22.56)	0.33	0.19	0.18	0.30
7H-2 (28.16)	0.33	0.19	0.18	0.34
10H-2 (30.47)	0.33	0.19	0.18	0.31
11H-5 (32.00)	0.33	0.19	0.18	0.31
12H-1 (32.39)	0.33	0.19	0.18	0.32
12H-5 (33.06)	0.33	0.19	0.18	0.32
13H-2 (33.71)	0.33	0.19	0.15	0.34
13H-3 (33.93)	0.33	0.20	0.18	0.33
13H-6 (35.33)	0.33	0.20	0.19	0.33

14H-2 (36.36)	0.33	0.19	0.19	0.33
14H-5 (37.18)	0.33	0.20	0.18	0.33
15H-1 (38.45)	0.34	0.19	0.18	0.32
16H-1 (39.91)	0.33	0.20	0.18	0.33
Sample	Component 1	Component 2	Component 3	Component 4
1218A (Ma)		Percentage (%)		
9H-1 (22.80)	16.8	61.4	15.8	5.9
11H-5 (25.82)	16.7	58.8	15.7	8.8
13H-7 (27.10)	15.8	59.4	16.8	7.9
19H-6 (30.48)	17.8	57.4	18.8	5.9
20H-6 (31.11)	16.8	59.4	17.8	5.9
23X-6 (33.70)	18.8	59.4	15.8	5.9
24X-7 (35.06)	18.8	69.3	7.9	4.0
26X-4 (38.20)	18.9	69.5	8.4	3.2
1218A (Ma)		$B_{1/2}$ (mT)		
9H-1 (22.80)	13.2	33.1	63.1	213.8
11H-3 (25.82)	13.5	32.4	64.6	218.8
13H-7 (27.10)	13.2	33.9	63.1	213.8
19H-6 (30.48)	13.5	33.9	63.1	213.8
20H-6 (31.11)	13.2	33.9	63.1	213.8
23X-6 (33.26)	13.2	31.6	64.4	218.8
24X-7 (35.06)	13.5	32.4	61.7	213.8
26X-4 (38.20)	13.2	32.4	61.7	218.8
1218A (Ma)		Dispersion parameter (DP)		
9H-1 (22.80)	0.34	0.19	0.18	0.34
11H-3 (25.82)	0.34	0.18	0.15	0.34
13H-7 (27.10)	0.33	0.19	0.15	0.34
19H-6 (30.48)	0.33	0.19	0.18	0.32
20H-6 (31.11)	0.32	0.18	0.18	0.33
23X-6 (33.26)	0.32	0.18	0.15	0.32
24X-7 (35.06)	0.32	0.19	0.15	0.34
26X-4 (38.20)	0.32	0.18	0.18	0.33

Table S2. BH/BS ratio from TEM results and IRM unmixing

Sample (Age)	TEM-BH	TEM-BS	TEM-BH/BS	IRM-BH	IRM-BS	IRM-BH/BS
9H-1（22.80）	0.206	0.794	**26%**	0.158	0.614	**26%**
19H-6（30.48）	0.217	0.783	**28%**	0.188	0.574	**33%**
26X-4（38.20）	0.103	0.897	**11%**	0.084	0.695	**12%**

References

Coxall, H.K., Wilson, P.A., Palike, H., Lear, C.H., and Backman, J., 2005, Rapid stepwise onset of Antarctic glaciation and deeper calcite compensation in the Pacific Ocean: Nature, v. 433, p. 53–57, https://doi.org/10.1038/nature03135.

Craig, A.P., Vertenstein, M., and Jacob, R., 2012, A new flexible coupler for earth system modeling developed for CCSM4 and CESM1. International Journal of High-Performance Computing Applications, v. 26, p. 31–42, https://doi.org/10.1177/1094342011428141.

Danabasoglu, G., Bates, S.C., Briegleb, B.P., Jayne, S.R., Jochum, M., Large, W.G., et al., 2012, The CCSM4 Ocean Component. Journal of Climate, v. 25, p. 1361–1389, https://doi.org/10.1175/Jcli-D-11-00091.1.

Egli, R., 2004, Characterization of individual rock magnetic components by analysis of remanence curves, 2. Fundamental properties of coercivity distributions: Physics and Chemistry of the Earth, v. 29, p. 851–867, https://doi.org/10.1016/j.pce.2004.04.001.

Goldner, A., Herold, N., and Huber, M., 2014, Antarctic glaciation caused ocean circulation changes at the Eocene–Oligocene transition: Nature, v. 511, p. 574–577, https://doi.org/10.1038/nature13597.

Gough, D.O., 1981, Solar interior structure and luminosity variations: Solar Physics, v. 74, p. 21–34, https://doi.org/10.1007/bf00151270.

Hunke, E., and Lipscomb, W., 2010, CICE: the Los Alamos Sea ice model user's manual, version 4: Tech. Rep. LA-CC-06-012 (Los Alamos National Laboratory, 2008).

Hutchinson, D K., Coxall, H.K., Lunt, D.J., Steinthorsdottir, M., and Zhang, Z., 2021, The Eocene–Oligocene transition: a review of marine and terrestrial proxy data, models and model–data comparisons: Climate of the Past, v. 17, p. 269–315. https://doi. org/10.5194/cp-2020-68.

Jacobel, A.W., McManus, J.F., Anderson, R.F., and Winckler, G., 2017, Repeated storage of respired carbon in the equatorial Pacific Ocean over the last three glacial cycles: Nature Communications, v. 8, p. 17-27, https://doi. org/doi:10.1038/s41467-017-01938-x.

Jian, Z., Dang, H., Yu, J., Wu, Q., Gong, X., Stepanek, C., et al., 2023, Changes in deep Pacific circulation and carbon storage during the Pliocene-Pleistocene transition: Earth and Planetary Science Letters, v. 605, p. 1–10, https://doi.org/10.1016/j.epsl.118020.

Lawrence, D.M., Oleson, K.W., Flanner, M.G., Fletcher, C.G., Lawrence, P.J., Levis, S., et al., 2012, The CCSM4 Land Simulation, 1850-2005: assessment of surface climate and new capabilities. Journal of Climate, v. 25, p. 2240–2260, https://doi.org/10.1175/Jcli-D-11-00103.1

Li, J., Liu, Y., Liu, S., Roberts, A.P., Pan, H., Xiao, T. and Pan, Y., 2020, Classification of a complexly mixed magnetic mineral assemblage in Pacific Ocean surface sediment by electron microscopy and supervised magnetic unmixing: Frontiers in Earth Science, v. 8, p. 1-18, https://doi.org/10.3389/feart.2020.609058.

Liu, Q.S., Yu, Y.J., Pan, Y.X., Zhu, R.X., Zhao, X.X., 2005, Partial anhysteretic remanent magnetization (pARM) of synthetic single- and multidomain magnetites and its paleoenvironmental significance: Chinese Science Bulletin. V. 50, p. 2381–2384. https://doi.org/10.1007/BF03183751

Mortlock, R.A., and Froelich, P.N., 1989, A simple method for the rapid determination of biogenic opal in pelagic marine sediments: Deep-Sea Research, v. 36, p. 1415–1426. https://doi. org/10.1016/0198-0149(89)90092-7.

Neale, R.B., Richter, J., Park, S., Lauritzen, P.H., Vavrus, S.J., Rasch, P.J., and Zhang, M.H., 2013, The mean climate of the Community Atmosphere Model (CAM4) in forced SST and fully coupled experiments: Journal of Climate, v. 26, p. 5150–5168. https://doi.org/10.1175/Jcli-D-12-00236.1

Pälike, H., et al., 2010, Proceedings of the Integrated Ocean Drilling Program, 320/321: Tokyo (Integrated Ocean Drilling Program Management International, Inc.). https://doi:10.2204/iodp.proc.320321.101.2010

Rae, J.W.B., Zhang, Y.G., Liu, X.Q., Foster, G.L., Stoll, H.M., and Whiteford, R. D. M., 2021, Atmospheric CO_2 over the past 66 million years from marine archives: Annual Review of Earth and Planetary Science, v. 49, p. 609–641, https://doi. org/10.1146/annurev-earth-082420-063026.

Roberts, A.P., Pike, C.R., and Verosub, K.L., 2000, First-order reversal curve diagrams: a new tool for characterizing the magnetic properties of natural samples: Journal of Geophysical Research: Solid Earth, v. 105, p. 28461–28475, https://doi.org/10.1029/2000JB900326.

Russell, J., 2023, Southern Ocean heat sink hindered by melting ice: Nature, v. 615, p. 799-800, https://doi.org/10.1038/d41586-023-00835-2.

Scotese, C. R. & Wright, N., 2018, PALEOMAP Paleodigital Elevation Models (PaleoDEMS) for the Phanerozoic (PALEOMAP Project); https://www.earthbyte.org/paleodem-resource-scotese-and-wright-2018/.

Taylor, S.R., and McLennan, S.M., 1985, The Continental Crust: Its Composition and Evolution: Malden, Massachusetts, Blackwell, 312 p.

Wang, D.F., Roberts, A.P., Rohling, E.J., Yao, W.Q., Zhong, Y., Yao, Z.Q., Lu, Y., and Liu, Q.S., 2023, Equatorial Pacific dust fertilization and source weathering influences on Eocene to Miocene global CO_2 decline: Communications Earth & Environment, v. 4, p. 1-9, https://doi.org/10.1038/s43247-023-00702-y.

Westerhold, T., Röhl, U., Wilkens, R., Pälike, H. and Expedition 320/321 Scientists, 2012, Revised composite depth scales and integration of IODP Sites U1331-U1334 and ODP Sites 1218-1220: Proceedings of the Integrated Ocean Drilling Program, https://doi.org/10.2204/iodp.proc.320321.201.2012.